remote sensing

MDPI

Article

Utilization of Hyperspectral Remote Sensing Imagery for Improving Burnt Area Mapping Accuracy

Michael Nolde *, Simon Plank and Torsten Riedlinger

German Aerospace Center (DLR), German Remote Sensing Data Center (DFD), Department for Geo-Risks and Civil Security, Oberpfaffenhofen, 82234 Wessling, Germany; simon.plank@dlr.de (S.P.); torsten.riedlinger@dlr.de (T.R.)

* Correspondence: michael.nolde@dlr.de

Abstract: Wildfires pose a direct threat when occurring close to populated areas. Additionally, their significant carbon and climate feedbacks represent an indirect threat on a global, long-term scale. Monitoring and analyzing wildfires is therefore a crucial task to increase the understanding of interconnections between fire and ecosystems, in order to improve wildfire management activities. This study investigates the suitability of 232 different red/near-infrared band combinations based on hyperspectral imagery of the DESIS sensor with regard to burnt area detection accuracy. It is shown that the selection of wavelengths greatly influences the detection quality, and that especially the utilization of lower near-infrared wavelengths increases the yielded accuracy. For burnt area analysis based on the Normalized Difference Vegetation Index (NDVI), the optimal wavelength range has been found to be 660–670 nm and 810–835 nm for the red band and near-infrared band, respectively.

Keywords: burnt area mapping; DESIS; hyperspectral imagery; NDVI; burn severity; active fire

Citation: Nolde, M.; Plank, S.; Riedlinger, T. Utilization of Hyperspectral Remote Sensing Imagery for Improving Burnt Area Mapping Accuracy. *Remote Sens.* **2021**, *13*, 5029. https://doi.org/ 10.3390/rs13245029

Academic Editor: Luke Wallace

Received: 9 November 2021
Accepted: 8 December 2021
Published: 10 December 2021

1. Introduction

Disastrous wildfires, such as the ones occurring in New South Wales/Australia in 2019/2020 or in California/USA in 2020, have gained wide recognition in the global media. While the endangerment of human lives and property is the primary point of concern, global wildfire activity is also a significant contributor to the greenhouse effect through CO_2 emissions, thus fostering global warming [1,2]. Studies showed that forest loss has increased substantially over the past two decades in many parts of the world, and that the underlying dynamics can be largely attributed to fire activity [3]. A better understanding of interactions between ecosystems, climate, humans and wildfire is therefore a constant aim in fire science [4].

Multispectral remote sensing allows the observation of large-scale fire activity patterns with high temporal resolution, which has significantly improved the knowledge in this domain in the past few decades. Monitoring wildfires using satellite-based Earth Observation imagery has become an essential tool for wildfire analysis and mitigation management.

The assessment of burnt areas through remote sensing imagery is usually based on a combination of information of either the red/near-infrared (NIR) or the near-infrared/short wave infrared (SWIR) domain. This is done by utilizing a normalized difference index such as the Normalized Difference Vegetation Index (NDVI) [5], or the Normalized Burn Ratio (NBR) [6], often through a comparison of different points in time. A comprehensive overview of burnt area mapping indices was compiled by Veraverbeke [7]. The concept of the exploitation of synergetic effects between burnt area indices and thermal anomaly data, which is also employed in this study, has been proposed by Fraser et al. and Li et al. [8,9].

The MCD64A1 [10] dataset by the National Aeronautics and Space Administration (NASA), and the Fire_cci BA 5.1 dataset [11] by the European Space Agency (ESA), represent the two most widely used, globally available burnt area datasets. Both are derived from

multispectral imagery of the moderate-resolution Imaging Spectroradiometer (MODIS) instrument onboard the NASA Aqua and Terra satellites. Another dataset, based on imagery of the Ocean and Land Color Instrument (OLCI) sensor onboard the ESA Sentinel-3A/B satellites, is currently prepared by the German Aerospace Center (DLR) [12]. This latter dataset comprises global burnt area data for recent years, and also near-realtime information in the form of a wildfire monitoring service. The service is available for the area of Europe, and is updated twice a day. It is developed and maintained by the department for Geo-Risks and Civil Security (GZS) of the German Remote Sensing Data Center (DFD) at DLR.

Recently, several hyperspectral instruments have been developed as part of spaceborne missions, such as the Hyperspectral Infrared Imager (HyspIRI) of the NASA, the Precursore Iperspettrale Della Missione Applicativa (PRISMA) of the Agenzia Spaziale Italiana (ASI), and the DLR Earth Sensing Imaging Spectrometer (DESIS) of the DLR. The Environmental Mapping and Analysis Program (EnMAP), another hyperspectral sensor developed by DLR, is scheduled to be launched in 2022. Contrary to multispectral sensors, which feature a small number of non-contiguous bands with a bandwidth wider than 20 nm, such hyperspectral instruments provide a multitude of spectrally contiguous bands with a bandwidth below 20 nm [4]. This high radiometric resolution can be leveraged to extract valuable information about vegetation type, biomass, chlorophyll, and leaf nutrient concentration. This, in turn, allows deeper insights into ecosystem functions, vegetation growth, and nutrient cycling than were formerly possible [13].

This study analyzes the suitability of each red/NIR band combination possible with the DESIS sensor bands regarding burnt area detection accuracy. Using the 4× binning variant of the product, this comprises eight bands in the red domain, which are located between between 624 and 705 nm, and 29 bands in the NIR domain, located between 705 and 1000 nm. The DESIS data are analyzed using the tested and proven methodology employed for the operation of the DLR-GZS wildfire monitoring service, as proposed by Nolde et al. [12]. The primary aim of the study is to identify the red/NIR band wavelength combination best suited for burnt area monitoring. These findings are applicable to other hyperspectral sensors, but also support the selection of suitable bands regarding multispectral sensors, such as Sentinel-3 OLCI.

2. Materials and Methods

The DESIS sensor provides information in the blue, green, red, and part of the NIR wavelengths. Pereira et al. stated that the NIR domain can be considered to be the best suited one for burnt area detection and mapping [14]. The same was found by Pleniou and Koutsias, who thoroughly investigated differences in spectral reflectance values between burnt and unburnt vegetation regarding various wavelengths. Their results showed that the red band features differences in signal strength twice as high compared to the blue and green band, while the NIR band even showed differences which were six times stronger [15]. Veraverbeke et al. compared 16 common spectral indices regarding burnt area detection accuracy. Of these, 15 utilized information from the NIR domain, while the red domain was used in eight indices. The blue band was used for one index only, and the green band was not used at all. Bands from longer wavelengths were used for 10 of the 16 investigated indices [7].

Since the blue and green wavelengths can be regarded as unsuited for the purpose of burnt area detection, this study is only concerned with the red and NIR domains of the spectrum offered by DESIS.

While the MCD64A1 and Fire_cci BA 5.1 datasets utilize information from different spectral ranges including the SWIR domain, the DLR-GZS monitoring service is restricted to red and NIR bands. This is due to the fact that Sentinel-3 OLCI only covers the spectral range from 385 nm to 1040 nm, which does not include the SWIR range [16]. The level 1 product comprises 21 bands with varying band widths (between 2.5 and 40 nm) in the visible and near-infrared wavelengths between 385 and 1040 nm. Only two of these bands,

numbers 8 and 17, are utilized in the final level 2 product. Band 8 covers the electromagnetic spectrum between 660 and 670 nm, while band 17 covers 855 to 875 nm [16].

Since the wildfire monitoring service must necessarily operate in near-realtime, the information is acquired from the level 1 product. The level 2 product is only available at a later point in time.

The service is based on bands 8 and 17 because they represent a suitable basis for general purpose applications including burnt area monitoring. Furthermore, selecting the bands of the level 1 data which are also included in level 2 allowed the flawless transition to this higher processing level, in cases when timeliness is not an issue. However, no inter-comparison of the available level 1 bands has been undertaken during the initial phase of the service development to ascertain that the selected bands really are the most suited ones for the purpose of burnt area monitoring.

This study undertakes this effort but uses a more comprehensive approach. Firstly, it identifies the optimal wavelengths for burnt area detection within the red and NIR domain, using hyperspectral data with high radiometric resolution. Consecutively, this range is compared to the range of the Sentinel-3 OLCI bands currently used in the wildfire monitoring service, to determine if using different bands from the OLCI level 1 product would be beneficial.

The DESIS instrument features an radiometric coverage of the electromagnetic range from 402 nm to 1000 nm, and thus almost entirely covers the range from the lower limit in band 1 to the upper limit in band 21 of the OLCI instrument (385 and 1040 nm, respectively). This circumstance makes DESIS well suited for this kind of analysis. The DESIS sensor is operated by Teledyne Brown Engineering/USA, and the DLR [17]. It is integrated within the Multi-User-System for Earth Sensing (MUSES) platform, which is installed on the International Space Station (ISS). Its intended fields of application primarily are the analysis of vegetation health and stress, water quality and pollution as well as the Earth's mineral resources. The instrument is built as a pushbroom imaging spectrometer, with a ground sampling distance of 30 m at nadir and a swath width of about 30 km. Table 1 lists a selection of the sensor's technical specifications.

Table 1. DESIS design specifications, from Müller et al. [18], edited.

	Instrument Design Parameters
Telescope F#/Focal length	3/320 mm, telecentric
Field of View	4.4°
Instantaneous Field of View	0.004°
Ground Sample Distance (nadir)	30 m (reference flight altitude: 400 km)
Swath (nadir)	~30 km (reference flight altitude: 400 km)
Spectral range	400–1000 nm
Spectral sampling	2.55 nm/235 bands
Number of spectral channels	235 (no binning) 117 (2× binning) 78 (3× binning) 58 (4× binning)

The methodology of this study follows an approach sometimes referred to as the so-called "brute force approach". In this context, this means that every single possible wavelength combination in the red and near-infrared domain is analyzed regarding its suitability for burnt area derivation. Each result is evaluated using a variety of common metrics. This proceeding is performed regarding each DESIS scene available for the study area.

To evaluate the performance, the results are compared against a reference, for which the Sentinel-3 based DLR-GZS wildfire monitoring service is utilized. To ensure that differences in results can clearly be attributed to the differing inputs, the DESIS data are analyzed following the exact methodology of the wildfire monitoring service. This

methodology is shown in Figure 1 and briefly described consecutively. An extensive documentation can be found in the literature [12].

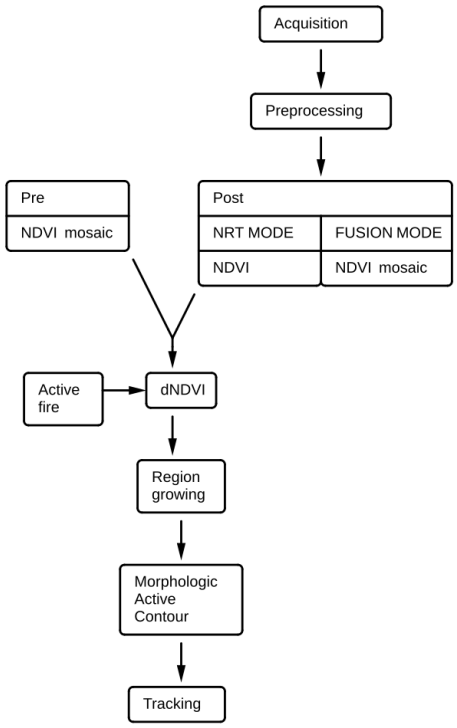

Figure 1. Schematic workflow for the burnt area derivation, from Nolde et al. [12].

The methodology has primarily been designed for monitoring continental scale regions in near-real time. However, it can as well be applied to archived data in order to perform retrospective time series analyses. The generated product contains the exact perimeter of each burnt area, as well as the date of detection, and the burn severity by means of the differential NDVI ($NDVI_{diff}$, see Equations (1) and (2), respectively).

$$NDVI = \frac{NIR - Red}{NIR + Red} \tag{1}$$

$$NDVI_{diff} = NDVI_{pre} - NDVI_{post} \tag{2}$$

The burnt area derivation method basically exploits the synergetic effects of information from the red and NIR wavelengths, combined through the application of the NDVI.

The pre-processing includes the preparation of pre- and post NDVI mosaics, from which the $NDVI_{diff}$ is calculated as a basis for the segmentation algorithm. The generation of the pre-mosaic is initialized with the earliest available scene for the area of interest within a 30 day time range before the post scene date. Sections either not covered or affected by clouds in this area are then progressively complemented with cloud-free information from more recent scenes. The generation of the post-mosaic is performed accordingly, with the difference that pixels featuring low NDVI values are overwritten by pixels with higher values in consecutive scenes. This is done in order to mitigate false detections due to cloud shadows. In addition, the utilized time range is shorter compared to the pre-mosaic.

To segment a given area into burnt and unburnt portions, the concept of Morphological Active Contours without Edges (MorphACWE) [19,20] is utilized. This method is closely related to Geodesic Active Contour Level Sets [21]. The algorithm generates a dynamic curve, which grows starting from seed locations and converges when an optimal segmentation of the actual burnt area is reached. This proceeding was shown to yield

results of high geometric accuracy when having been inter-compared with the NASA MCD64A1 dataset [12].

As seed information, thermal anomaly locations from the MODIS MOD14A1/MYD14A1 product [22] as well as the Visible Infrared Imaging Radiometer Suite (VIIRS) VNP14A1 product [23] are used.

Both products are based on a contextual algorithm, which utilizes brightness temperature differences between the mid-infared (MIR) and thermal infrared (TIR) domain to identify biomass burning locations [24,25]. While the MODIS product is available with a spatial resolution of 1 km, the product based on VIIRS features a ground resolution of 375 m at nadir.

This study analyses which wavelength ranges in the red and NIR domain are best suited for the task of burnt area derivation. A substantial obstacle for this kind of study is source data scarcity. DESIS does not continuously monitor the Earth's surface, but needs to be tasked for each desired data acquisition. Studies incorporating a multitude of input scenes thus require careful acquisition planning and execution, or need to be based on already available, archived data.

For this study, information from different points in time is required due to the pre/post-approach used in the derivation methodology. Ideally, these time steps should be located in close temporal proximity to the actual fire event, with the pre scene being acquired shortly before and the post scene shortly after a fire. Furthermore, an extended geographical region should be covered, in order to enable the derivation of statistically relevant performance indicators.

Preconditions for the selection of the study region were thus the availability of DESIS data with sufficient geographic and temporal extent, and the presence of significant fire activity. To that purpose, the DLR EOWEB GeoPortal [26] was inspected for DESIS data in regions regularly affected by wildfires. The region of Northern California could finally be established as a suitable study site. This region experienced dramatic wildfire outbreaks in the 2020 fire season, particularly in the month of August. In total, 56 DESIS scenes are available for the site, distributed over the time range from 2018 to 2021. The area of interest, together with geometric footprints of the available DESIS scenes, is depicted in Figure 2.

An exemplary pair of a pre and a post scene, both partly overlapping a huge burnt area in the western part of the area of interest, is shown in Figure 3. The red, green and blue channels have been used for visualisation, instead of the red and NIR channels utilized for the actual analysis. The pre scene was acquired on 9 June 2020 and the post scene on 8 April 2021. The Sentinel-3 based burnt area reference is depicted in dark gray in the background, with the outline shown additionally in orange above the DESIS scenes. The post scene, placed above the pre scene, shows darkened areas caused by burning within the area indicated by the reference. The large temporal distance between the two DESIS scenes is due to the scarcity of available DESIS data. A value of 12 months was chosen as the maximal allowed distance between pre and post scenes in this study.

The DESIS level 2A product is available in its original form, as well as three post-processing variants. The original variant provides a totality of 235 bands, each covering a wavelength range of 2.55 nm [27]. The other variants are binning products, for which several bands are combined. These post-processed products feature an improved signal-to-noise ratio. For this study, all available 56 scenes for northern California were retrieved in their 4× binning variant, which contains 58 bands.

Eight of these bands, the ones with numbers 22 to 29, belong to the red domain. They feature wavelength centers from 629.5 to 700.9 nm. The bands with numbers 30 to 58 are attributed to the NIR domain. Their wavelength centers range from 711.1 to 996.7 nm.

To identify the band combination with the most favorable properties regarding burnt area derivation, each available red band is combined with each NIR band. This results in 232 (8 red * 29 NIR) combinations for each individual hyperspectral scene of the scenes available. Since 56 scenes are used, this yields a totality of 12,992 multispectral input variants for the processing. Every single combination is used to calculate the respective NDVI. The

$NDVI_{diff}$, calculated from the NDVI of a pre and a post scene, operates consecutively as an input for the burnt area processing mechanism.

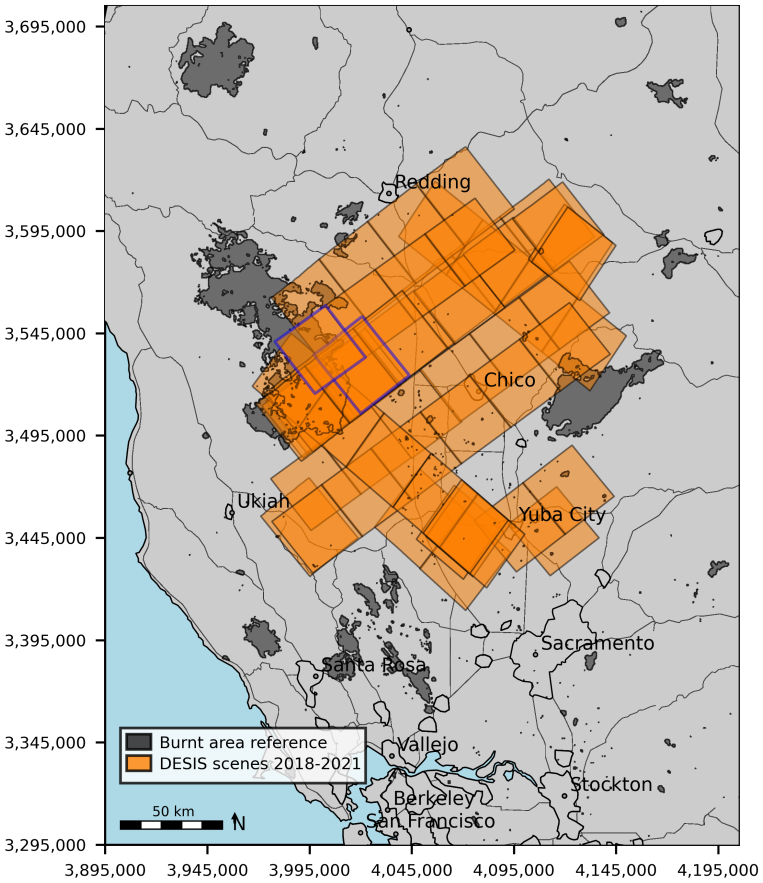

Figure 2. Area of Interest: Northern California. The footprints of available DESIS scenes are shown in orange. Burnt area reference perimeters, derived from Sentinel-3 OLCI data, are depicted in dark gray. The footprints with blue contours depict the region exemplary visualized in Figure 3.

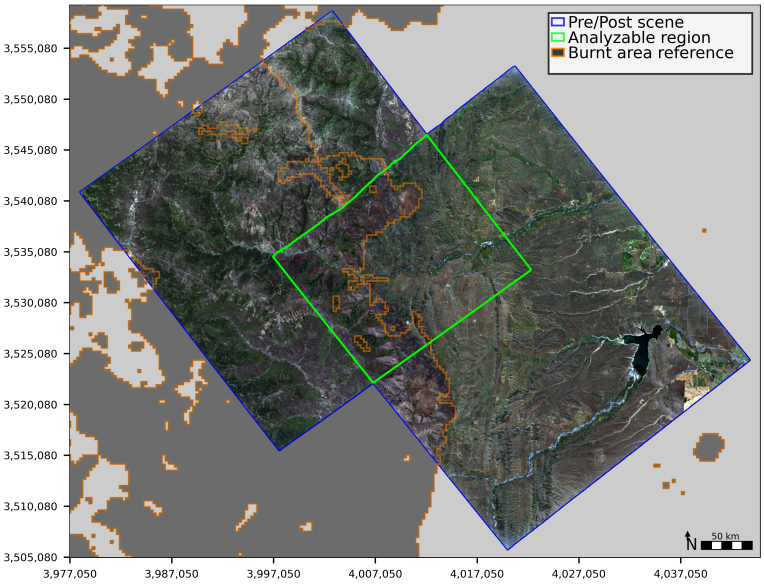

Figure 3. Exemplary pre scene (left) and post scene (right) from 9 June 2020, and 8 April 2021, respectively.

3. Results

Exemplary results for two different red/NIR band combinations are shown in Figure 4. The red/NIR band combinations used are 22/30 and 25/40.

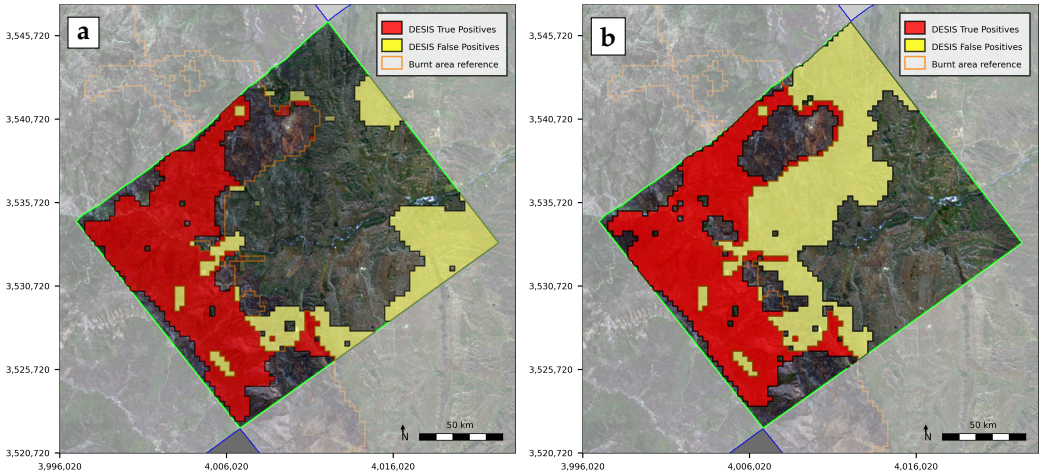

Figure 4. Results utilizing different red/NIR combinations. Subfigure (**a**) depicts the results gained with combination 22/30, while subfigure (**b**) shows the results for combination 25/40 (4× binning).

The term True Positives (TP_{pix}) subsequently refer to the number of burnt area pixels which are derived for a specific DESIS band combination regarding a single scene, which overlap with the burnt area pixels contained in the Sentinel-3 OLCI reference. Consecutively, the term False Positives (FP_{pix}) addresses the number of derived burnt area pixels which do not overlap with the burnt area pixels in the reference. For the accuracy assessment, these values are set in relation to the number of total burnt area pixels in the reference, in the form of a ratio.

It can be seen in Figure 4 that both combinations yield very similar results regarding the True Positives, meaning that they cover most parts of the reference area. However, they feature extensive differences regarding the falsely determined area (False Positives). The metric primarily used in this study to evaluate the quality of the results combines these two factors, by building the average of the True Positive ratio and the inverse False Positive ratio. Equation (3) shows the determination of the TP/FP_{inv} value for a single scene. Equation (4) illustrates the weighting of the individual results by integrating the size of the reference burnt area in each scene. The ratios are calculated based on the respective sums of True Positive pixels, False Positive pixels, and Reference burnt area pixels regarding all scenes. This results in a weighted average value. If the accuracy for each scene would be determined individually instead and then consecutively used to calculate an "average of averages", the scenes with a small number of burnt area pixels would be greatly over-represented, and thus the result would be significantly distorted.

$$TP/FP_{inv} = \frac{\frac{TP_{pix}}{Ref_{pix}} + (1 - \frac{FP_{pix}}{Ref_{pix}})}{2} \tag{3}$$

$$\overline{TP/FP_{inv}} = \frac{\frac{\sum TP_{pix}}{\sum Ref_{pix}} + (1 - \frac{\sum FP_{pix}}{\sum Ref_{pix}})}{2} \tag{4}$$

The yielded weighted averages regarding all 232 band combinations for each of the 56 scenes regarding the TP/FP_{inv} metric are depicted in Table 2. To allow a more complete overview, the evaluation is also performed with a variety of alternative metrics, namely the F1-Score, Intersect over Union, Accuracy, Kohen's Kappa, Precision, and Recall. Since each metric weights the inputs of True Positives and False Positives differently, the results vary within a reasonable range.

Each cell in Table 2 represents the accuracy result for a specific red/NIR band combination. As can be seen, the highest accuracy achieved is 0.74, while the lowest is 0.6.

Several regions are specifically expressive, and are thus highlighted with black and colored boundaries, respectively: The black rectangle circumscribes the red/NIR wavelengths used in the bands 8 and 17 contained in the Sentinel-3 OLCI level 2 product. As stated, these are also the bands utilized as a basis for the DLR-GZS wildfire monitoring service. The corresponding accuracy results using DESIS band information yields an average value of 0.67, meaning an accuracy of 67%.

The blue rectangle shows the best available alternative, when the same red/NIR wavelength width is postulated. The rectangle depicts the optimal wavelengths indicated with the TP/FP_{inv}, F1-Score and Intersect over Union metrics. Using these wavelengths, corresponding to the DESIS bands 40–42 in the NIR and 25/26 in the red domain, results in an averaged accuracy value of 0.72, indicating a performance gain of 5%. The further, dotted rectangles depict the regions identified when other metrics are used. The violet box marks the optimal wavelengths according to the Accuracy and Cohen's Kappa metrics. Cyan refers to the Precision metric, while dark blue addresses the Recall.

Table 2. Accuracy results for each red/NIR band combination, derived using the TP/FP_{inv} metric. The cell values represent the total accuracy of all 56 input scenes. The colored rectangles indicate the optimal wavelengths for burnt area detection according to different metrics, while the black rectangle marks the region of the Sentinel-3 OLCI bands used in the DLR-GZS wildfire monitoring service.

	22 (629.5)	**23** (639.7)	**24** (649.9)	**25** (660.1)	**26** (670.3)	**27** (680.5)	**28** (690.7)	**29** (700.9)
30 (711.1)	0.7	0.7	0.73	0.69	0.67	0.73	0.64	0.66
31 (721.3)	0.7	0.66	0.64	0.68	0.68	0.65	0.73	0.65
32 (731.5)	0.64	0.68	0.66	0.68	0.65	0.69	0.69	0.7
33 (741.7)	0.67	0.69	0.72	0.68	0.68	0.68	0.72	0.71
34 (751.9)	0.72	0.67	0.69	0.67	0.69	0.69	0.68	0.69
35 (762.1)	0.72	0.71	0.7	0.68	0.67	0.66	0.69	0.7
36 (772.3)	0.72	0.7	0.71	0.71	0.69	0.71	0.68	0.7
37 (782.5)	0.7	0.72	0.69	0.67	0.7	0.69	0.72	0.69
38 (792.7)	0.71	0.71	0.7	0.71	0.67	0.72	0.68	0.7
39 (802.9)	0.73	0.72	0.73	0.72	0.72	0.69	0.67	0.7
40 (813.1)	0.68	0.72	0.7	0.72	0.69	0.71	0.69	0.69
41 (823.3)	0.69	0.73	0.68	0.73	0.73	0.74	0.68	0.67
42 (833.5)	0.71	0.72	0.69	0.74	0.72	0.67	0.69	0.7
43 (843.7)	0.66	0.67	0.7	0.7	0.63	0.71	0.7	0.72
44 (853.9)	0.7	0.72	0.67	0.72	0.69	0.72	0.65	0.71
45 (864.1)	0.66	0.69	0.65	0.65	0.66	0.72	0.68	0.68
46 (874.3)	0.66	0.67	0.66	0.65	0.64	0.68	0.68	0.69
47 (884.5)	0.63	0.64	0.65	0.65	0.62	0.68	0.66	0.65
48 (894.7)	0.64	0.64	0.64	0.63	0.65	0.67	0.66	0.64
49 (904.9)	0.67	0.65	0.64	0.64	0.67	0.72	0.68	0.68
50 (915.1)	0.66	0.66	0.69	0.68	0.68	0.7	0.68	0.7
51 (925.3)	0.65	0.68	0.63	0.63	0.67	0.7	0.69	0.71
52 (935.5)	0.61	0.61	0.65	0.6	0.63	0.64	0.67	0.66
53 (945.7)	0.65	0.68	0.65	0.68	0.68	0.69	0.71	0.71
54 (955.9)	0.67	0.71	0.66	0.71	0.67	0.7	0.7	0.7
55 (966.1)	0.66	0.65	0.65	0.7	0.69	0.66	0.72	0.66
56 (976.3)	0.64	0.65	0.69	0.64	0.66	0.66	0.69	0.69
57 (986.5)	0.66	0.67	0.67	0.66	0.64	0.65	0.67	0.66
58 (996.7)	0.65	0.66	0.67	0.65	0.66	0.62	0.64	0.67

Table 3 provides an overview of the utilized metrics, listing the derived optimal wavelengths together with the metric's average value for the identified spectral range.

Table 3. Optimally suited wavelengths for burnt area detection, regarding different metrics.

Metric	Color	Optimal Wavelength Range (nm)		Average Score for Optimal Red/NIR Wavelength Range
		Red Domain	NIR Domain	
TP/FP_{inv}		655.0–675.4	808.0–838.6	0.721
F1-Score		655.0–675.4	808.0–838.6	0.703
Intersect over Union		655.0–675.4	808.0–838.6	0.542
Accuracy		634.6–655.0	777.7–808.0	0.779
Cohen's Kappa		634.6–655.0	777.7–808.0	0.524
Precision		624.4–644.8	797.8–828.4	0.759
Recall		655.0–675.4	757.0–787.6	0.685

4. Discussion

The scarcity of the DESIS data can be regarded as the biggest problem in preparing a study of this kind. While the DLR-GZS wildfire monitoring service profits from Sentinel-3 OLCI data being provided twice a day for the area of Europe, DESIS data are only available for dates and regions the sensor was specifically tasked for. For the existing scenes, a corresponding earlier scene which could be used for pre information is often unavailable. Even if this is the case, the temporal distance between pre and post scene might span several months or even years. For the presented task of wildfire burnt area monitoring, this circumstance represents a considerable obstacle, since vegetation affected by fire will in most cases recover over extended time periods, which prohibits the derivation of accurate burnt area perimeters. This can be seen in Figure 4, where an exact reproduction of the reference perimeter was not possible with both depicted band combinations. A large region in the northern half of the analyzable area has recovered so completely that it was evaluated in both cases as not being affected by fire at all. While the initial conditions for this kind of analysis are not optimal, however, these same conditions apply to all analyzed red/NIR band combinations in the same way. This study shows which combinations yield better results under difficult circumstances than others, and thus still allows the drawing of robust conclusions. With data from further hyperspectral sensors such as PRISMA and EnMAP being available, the problem of data scarcity will diminish in the near future.

Since DESIS products are offered in four variants, the original version together with three binning products, the question arises as to which of the products provides the most beneficial properties for analyses. While the original variant offers the highest radiometric resolution, Müller et al. could show that it has a comparatively low signal-to-noise (SNR) ratio. The SNR of the 4× binning product is almost twice as high compared to the original version for nearly all wavelengths [18]. This study therefore uses to 4× binning variant, in which groups of four bands are aggregated into one, thus significantly improving the SNR.

Table 2 enables a straightforward comprehension of the achieved results. The coloring, firstly, shows that it is of considerable importance which wavelengths of the red and NIR spectra are used for the task of burnt area derivation. The accuracy values range from 60% to 74%. A color gradient is discernible from the lower right to the upper left corner, showing a transition from lower to higher accuracy values. This indicates that wavelengths in the lower part of the NIR spectrum, between 700 to 850 nm, are clearly better suited for the task than higher wavelengths. A similar, while less distinguished trend can be observed for the red spectrum, where the analyses based on wavelengths between 630 and 670 nm yielded slightly better results compared to higher wavelengths. Based on the utilized DESIS data, it can be stated that the combination of these mentioned ranges for red and NIR information is the preferable choice for the NDVI based derivation of burnt area information. It is interesting to note that three of the employed seven metrics coincide in the indication of the optimal wavelengths, while the remaining four metrics propose three slightly different regions. However, they are all in accordance with indicating that the lower parts of the red and NIR spectrum, respectively, are superior to the remaining wavelengths for the given task.

5. Conclusions

This study analyzes the suitability of various red/NIR band combinations from the DESIS sensor regarding wildfire burnt area detection accuracy. Fifty-six hyperspectral scenes are each subdivided into 232 band combinations, yielding a data basis of 12,992 multispectral input datasets. These are analyzed using a tested and proven methodology, which is used in the DLR-GZS wildfire monitoring service for burnt area detection with Sentinel-3 OLCI. The most accurate results are achieved when the wavelengths from 660 to 670 nm are used for the red band (corresponding to DESIS bands 25/26 with 4× binning) and 810 to 835 nm for the NIR band (DESIS bands 40–42). The accuracy for this combination is calculated to be 72% on average. While the optimal red band wavelength coincides with the one already used in the DLR-GZS wildfire monitoring service, which is based on Sentinel-3 OLCI data, the optimal NIR range differs from the one currently in operation. The accuracy gained with the proposed NIR wavelength is increased by 5% compared to the current setting. Since the OLCI sensor does not feature a NIR band in this better suited wavelength region, however, this range cannot be leveraged in the monitoring service. However, the results of this study are generally applicable to multispectral and hyperspectral sensors featuring the proposed wavelengths.

Author Contributions: Conceptualization, M.N., S.P. and T.R.; methodology, M.N.; software, M.N.; validation, M.N. and S.P.; formal analysis, M.N.; investigation, M.N.; resources, M.N.; data curation, M.N.; writing—original draft preparation, M.N.; writing—review and editing, M.N., S.P. and T.R.; visualization, M.N.; supervision, T.R.; project administration, M.N., S.P. and T.R.; funding acquisition, T.R. All authors have read and agreed to the published version of the manuscript.

Funding: This research received no external funding.

Institutional Review Board Statement: Not applicable.

Informed Consent Statement: Not applicable.

Data Availability Statement: DESIS hyperspectral data can be obtained through the DLR-EOC EOWEB® GeoPortal (https://eoweb.dlr.de/egp, accessed on 12 September 2021). A registration is required for downloading the scenes. Sentinel-3 OLCI L1 data are available via the Copernicus Open Access Hub (https://scihub.copernicus.eu, accessed on 20 June 2021).

Conflicts of Interest: The authors declare no conflict of interest.

References

1. Withey, K.; Berenguer, E.; Palmeira, A.F.; Espírito-Santo, F.D.; Lennox, G.D.; Silva, C.V.; Aragao, L.E.; Ferreira, J.; França, F.; Malhi, Y.; et al. Quantifying immediate carbon emissions from El Niño-mediated wildfires in humid tropical forests. *Philos. Trans. R. Soc. B Biol. Sci.* **2018**, *373*, 20170312. [CrossRef] [PubMed]
2. Surawski, N.; Sullivan, A.; Roxburgh, S.; Polglase, P. Estimates of greenhouse gas and black carbon emissions from a major Australian wildfire with high spatiotemporal resolution. *J. Geophys. Res. Atmos.* **2016**, *121*, 9892–9907. [CrossRef]
3. van Wees, D.; van der Werf, G. The contribution of fire to a global increase in forest loss. In Proceedings of the EGU General Assembly Conference Abstracts, Vienna, Austria, 4–8 May 2020; p. 18049.
4. Veraverbeke, S.; Dennison, P.; Gitas, I.; Hulley, G.; Kalashnikova, O.; Katagis, T.; Kuai, L.; Meng, R.; Roberts, D.; Stavros, N. Hyperspectral remote sensing of fire: State-of-the-art and future perspectives. *Remote Sens. Environ.* **2018**, *216*, 105–121. [CrossRef]
5. Rouse, J.W.; Haas, R.H.; Schell, J.A.; Deering, D.W.; Harlan, J.C. Monitoring the vernal advancement and retrogradation (green wave effect) of natural vegetation. In *NASA/GSFC Type III Final Report*; NASA/GSFC: Greenbelt, MD, USA, 1974; Volume 371.
6. Key, C.H.; Benson, N.C. Measuring and remote sensing of burn severity. In Proceedings of the Joint Fire Science Conference and Workshop, University of Idaho and International Association of Wildland Fire, Boise, ID, USA, 15–17 June 1999; Volume 2, p. 284.
7. Veraverbeke, S.; Harris, S.; Hook, S. Evaluating spectral indices for burned area discrimination using MODIS/ASTER (MASTER) airborne simulator data. *Remote Sens. Environ.* **2011**, *115*, 2702–2709. [CrossRef]
8. Fraser, R.; Li, Z.; Cihlar, J. Hotspot and NDVI differencing synergy (HANDS): A new technique for burned area mapping over boreal forest. *Remote Sens. Environ.* **2000**, *74*, 362–376. [CrossRef]
9. Li, Z.; Nadon, S.; Cihlar, J.; Stocks, B. Satellite-based mapping of Canadian boreal forest fires: evaluation and comparison of algorithms. *Int. J. Remote Sens.* **2000**, *21*, 3071–3082. [CrossRef]
10. Giglio, L.; Justice, C.; Boschetti, L.; Roy, D. MCD64A1 MODIS/Terra+Aqua Burned Area Monthly l3 Global 500 m sin Grid v006 [Data Set]. 2015. Available online: https://doi.org/10.5067/MODIS/MCD64A1.006 (accessed on 12 October 2021).

11. Lizundia-Loiola, J.; Otón, G.; Ramo, R.; Chuvieco, E. A spatio-temporal active-fire clustering approach for global burned area mapping at 250 m from MODIS data. *Remote Sens. Environ.* **2020**, *236*, 111493. [CrossRef]
12. Nolde, M.; Plank, S.; Riedlinger, T. An Adaptive and Extensible System for Satellite-Based, Large Scale Burnt Area Monitoring in Near-Real Time. *Remote Sens.* **2020**, *12*, 2162. [CrossRef]
13. Im, J.; Jensen, J.R. Hyperspectral remote sensing of vegetation. *Geogr. Compass* **2008**, *2*, 1943–1961. [CrossRef]
14. Pereira, J.M.; Sá, A.C.; Sousa, A.M.; Silva, J.M.; Santos, T.N.; Carreiras, J.M. Spectral characterisation and discrimination of burnt areas. In *Remote Sensing of Large Wildfires*; Springer: Berlin/Heidelberg, Germany, 1999; pp. 123–138.
15. Pleniou, M.; Koutsias, N. Sensitivity of spectral reflectance values to different burn and vegetation ratios: A multi-scale approach applied in a fire affected area. *ISPRS J. Photogramm. Remote Sens.* **2013**, *79*, 199–210. [CrossRef]
16. European Space Agency/ESA. Sentinel-3 OLCI Introduction. 2020. Available online: https://sentinel.esa.int/web/sentinel/user-guides/sentinel-3-olci (accessed on 20 September 2021).
17. German Aerospace Center/DLR. DESIS Mission. 2021. https://www.dlr.de/eoc/desktopdefault.aspx/tabid-13614/ (accessed on 20 September 2021).
18. Müller, R.; Avbelj, J.; Carmona, E.; Gerasch, B.; Graham, L.; Günther, B.; Heiden, U.; Kerr, G.; Knodt, U.; Krutz, D.; et al. The new hyperspectral sensor DESIS on the multi-payload platform MUSES installed on the ISS. *Int. Arch. Photogramm. Remote Sens. Spat. Inf. Sci.* **2016**, *41*, 461–467. [CrossRef]
19. Chan, T.; Vese, L. An active contour model without edges. In *Proceedings of the International Conference on Scale-Space Theories in Computer Vision*; Springer: Berlin/Heidelberg, Germany, 1999; pp. 141–151.
20. Chan, T.F.; Vese, L.A. Active contours without edges. *IEEE Trans. Image Process.* **2001**, *10*, 266–277. [CrossRef]
21. Caselles, V.; Kimmel, R.; Sapiro, G. Geodesic active contours. In Proceedings of IEEE International Conference on Computer Vision, Cambridge, MA, USA, 20–23 June 1995; pp. 694–699.
22. Giglio, L.; Justice, C. MOD14A2 MODIS/Terra Thermal Anomalies/Fire 8-Day l3 Global 1 km sin Grid v006 [Data Set]. 2015. Available online: https://doi.org/10.5067/MODIS/MOD14A2.006 (accessed on 5 October 2021).
23. Schroeder, W.; Giglio, L. VIIRS/NPP Thermal Anomalies/Fire Daily l3 Global 1 km sin Grid v001 [Data Set]. 2017. Available online: https://doi.org/10.5067/VIIRS/VNP14A1.001 (accessed on 5 October 2021).
24. Giglio, L.; Descloitres, J.; Justice, C.O.; Kaufman, Y.J. An enhanced contextual fire detection algorithm for MODIS. *Remote Sens. Environ.* **2003**, *87*, 273–282. [CrossRef]
25. Schroeder, W.; Oliva, P.; Giglio, L.; Csiszar, I.A. The New VIIRS 375 m active fire detection data product: Algorithm description and initial assessment. *Remote Sens. Environ.* **2014**, *143*, 85–96. [CrossRef]
26. German Aerospace Center/DLR. EOC EOWEB GeoPortal. 2021. Available online: https://eoweb.dlr.de/egp (accessed on 5 October 2021).
27. Carmona, E.; Avbelj, J.; Alonso, K.; Bachmann, M.; Cerra, D.; Eckardt, A.; Gerasch, B.; Graham, L.; Günther, B.; Heiden, U.; et al. Data processing for the space-based DESIS hyperspectral sensor. *Int. Arch. Photogramm. Remote Sens. Spatial Inf. Sci.* **2017**, *42*, 271–277. [CrossRef]